Journal of Zhejiang University-SCIENCE A (Applied Physics & Engineering) 2024 25(12):974-990
www.jzus.zju.edu.cn; www.springer.com/journal/11582
E-mail: jzus_a@zju.edu.cn

Research Article

https://doi.org/10.1631/jzus.A2400018

Effect of dry–wet cycles on the mechanical properties and microscopic characteristics of fine breccia soil from karst areas

Xin LI[1,2,3], Hanqing CHEN[1,2,3]✉, Dong SU[1,2,3], Xiangsheng CHEN[1,2,3], Xiang SHEN[1,2,3]

[1]*Underground Polis Academy, College of Civil and Transportation Engineering, Shenzhen University, Shenzhen 518060, China*
[2]*Key Laboratory of Coastal Urban Resilient Infrastructures (Shenzhen University), Ministry of Education, Shenzhen 518060, China*
[3]*Shenzhen Key Laboratory of Green, Efficient, and Intelligent Construction of Underground Metro Station, Shenzhen 518060, China*

Abstract: The quality of the railway subgrade is directly related to the fill soil structure, which, in turn, is determined by the local physical and chemical environment. A karst environment, with its frequent rainfall, promotes the dissolution of soluble rocks and underground transportation of solutes, altering the soil structure and performance. To investigate these alterations, we analyzed the properties of underground soil from highly developed karst areas. Fine breccia soil from karst regions was tested to assess its macroscopic mechanical properties and microstructural features, for differing initial water contents and compaction levels. Samples were subjected to simulated rainfall conditions through dry–wet cycles, and then underwent triaxial shear and electron microscopy tests. From these data, a micro-to-macro correlation model and a normalization model were developed. The findings suggest that the resistance of fine angular breccia soil to degradation during dry–wet cycles can be enhanced through high-pressure compaction and by maintaining a moisture content close to 15.6%. Increasing the degree of compaction improves the particle size distribution and the density of the soil skeleton. This is advantageous for minimizing soil particle erosion, thereby ensuring the strong performance of railway subgrades in karst areas with frequent rainfall.

Key words: Karst area; Micro–macro properties; Railway subgrade performance; Dry–wet cycles

1 Introduction

Effective utilization of land resources and sustainable construction are paramount in railway engineering. In particular, railway subgrade construction aims to use locally sourced materials for excavation and filling. The quality of railway subgrade engineering is directly related to the fill soil, which is determined by the local physical and chemical environment, and is therefore region-specific (Xiao et al., 2007; Xu et al., 2019; Sun et al., 2021; Ibrahim et al., 2022; Raja et al., 2022; Wang SJ et al., 2022). Karst areas are unique ecological settings featuring wide distributions of underground soluble rocks, and complex interactions between surface and groundwater environments. A karst water environment promotes the dissolution of soluble rocks, the transportation and deposition of underground substances, and other processes that alter soil structure and performance (Smirnova and Gennadiev, 2011; Wang, 2014; Deng et al., 2020; Li et al., 2021). Notably, these factors are present even after filling and operation. After the underground soil in karst areas is used for railway subgrade fill, the project will still be subjected to a rainfall-intensive karst environment. Given the long-term influence of repeated rainfall infiltration and underground karst water seepage-induced erosion on the performance of railway subgrade soil, the effect of dry–wet cycles on the mechanical and deformation characteristics of soil in karst areas is of high practical significance (Mu et al., 2016; Celauro et al., 2017; Lu et al., 2020; Geng et al., 2022). However, as macroscopic performance is closely related to microstructural characteristics, the interpretation of macroscopic changes from a microscopic perspective can help us better understand the characteristics of railway subgrade soil structures and the mechanical properties of railway subgrade in karst areas (Jiang, 2019; Luo et al., 2022).

✉ Hanqing CHEN, hanqingchen@suz.edu.cn
Hanqing CHEN, https://orcid.org/0000-0002-2115-3538

Received Jan. 12, 2024; Revision accepted Aug. 12, 2024;
Crosschecked Dec. 1, 2024

The durability- and strength-related characteristics of railway subgrade fill materials must be evaluated to assess their usability. The inherent characteristics of soils formed under different conditions and their long-term performance in complex environments are important factors affecting railway subgrade quality (Zhou, 2012; Song et al., 2015; Han et al., 2016; Xu et al., 2019; Feng and Lei, 2022; Khalid et al., 2022). Consequently, the characteristics and long-term performance of karst soil should be investigated so as to improve its performance as railway subgrade fill.

The performance of railway subgrade fill and the durability of filled railway subgrade have been investigated extensively in different areas. Scholars have analyzed the macro-mechanical properties and microscopic structures of varying types of railway subgrade fill, including performance soils, blended soils, soils from unique regions, and recycled fine-particle waste materials. They have studied how the mechanical properties of various soils are affected by their chemical and physical compositions, and proposed corresponding mechanical models (Chen et al., 2019; Drobinina et al., 2020; Li Z et al., 2022; Que et al., 2022).

Numerous researchers have examined the evolution of the mechanical properties of soil under dry–wet cycles. For instance, Chao et al. (2023) studied the consolidated undrained triaxial shear characteristics of soil under the combined action of dry–wet cycles and vertical confining pressure; they found that the first dry–wet cycle had the largest impact on soil matric suction, while the vertical confining pressure could limit the impact of dry–wet cycles on the hydraulic properties of the soil. Other researchers have studied the shear strength, compressive properties, water–soil properties, participating strength, and tensile properties of sandy kaolin, coarse-grained soil, Guangxi clay, coal-bearing soil, and red clay under different dry–wet cycling conditions. Overall, these studies indicated that the initial dry–wet cycle typically has the greatest impact on soil properties (albeit with a certain lag), and showcased how corresponding damage constitutive equations could be established for different soils (Goh et al., 2014; Huang and Zheng, 2021; Wen et al., 2021; Li SY et al., 2022; Zeng et al., 2022). Fang et al. (2021) studied the effects of dry–wet cycles on the mechanical properties of expansive soil and discovered reductions in cohesion and the internal friction angle. Also, the suction friction angle after dry–wet cycles varied under suction conditions at or below 200 kPa and tended to stabilize after three cycles. In another study, Li et al. (2017) investigated the effect of dry–wet cycles on silty clay in highway railway subgrade and proposed a mechanism for the resulting damage. Also, Yu et al. (2019) studied the influence of dry–wet cycles on the shear strength and slope stability of granite residual soil and derived a corresponding safety factor for slope stability. They found that the shear strength stabilized after three to five cycles. Lu et al. (2020) combined the results of laboratory experiments and numerical simulations to model the long-term deformation of a railway subgrade exposed to traffic loads and dry–wet cycles; they divided the deformation into three stages with corresponding models. The results showed that the amplitude of the dry–wet cycles had a greater impact on railway subgrade deformation than confining pressure variation, suggesting that the range of variation in railway subgrade moisture content must be carefully controlled in practice.

Another focus of research has been explaining macroscopic mechanical phenomena from a microstructural perspective (Kong et al., 2022). As such, researchers have found correlations between microstructural parameters and macroscopic indicators. By using techniques such as triaxial testing, penetration testing, nuclear magnetic resonance, and scanning electron microscopy (SEM), several mechanisms have been elucidated (Lin and Cerato, 2015; Hong et al., 2020; Li and Liu, 2020; Hu et al., 2021; Yuan et al., 2021; Wang L et al., 2022).

Although some studies have dealt with special railway subgrade fill, soil property evolution in response to dry–wet cycles, and micro–macro soil mechanics, in-depth research on the mechanical properties and railway subgrade fill performance of in situ soil in karst areas is lacking. Additionally, research on the damage mechanisms and microscopic characteristics of soil subjected to dry–wet cycles in karst areas is scarce. Consequently, further investigation is needed to reveal the relevant mechanisms and provide guidance for railway subgrade filling projects in karst areas.

To address this research gap, we investigated the mechanical properties, microstructural characteristics, correlations between micro and macro characteristics, and damage characteristics of in situ railway subgrade fill in karst areas experiencing long-term dry–wet cycles. The subject of our analysis was underground

soil from mature karst areas. We conducted triaxial shear testing of soil samples with different moisture contents that were subjected to zero, two, four, and six dry–wet cycles, with each cycle involving 12 h of drying and 12 h of vacuum saturation. Experiments were conducted to obtain the failure strengths, elastic moduli, shear parameters, particle size distributions, and void particle ratios of soil samples under different conditions. We also propose a novel damage model for underground soil in karst areas subjected to dry–wet cycles. The results of the unconsolidated and undrained triaxial tests were used to analyze the macroscopic mechanical characteristics of the soil. SEM imaging and graphical feature extraction and quantification were conducted to examine the microscopic characteristics of karst soil under different conditions and provide suggestions for engineering practice.

2 Methodology

2.1 Materials

The soil used in this study is a natural fine breccia soil collected in Xinyu City of Jiangxi Province, China (a karst area), used as a fill for nearby railway subgrade projects. The soil collection area receives a large amount of rainfall and can be classified as a highly developed karst area, featuring soluble rocks and underground rivers, and characterized by frequent soil cave collapses. Soil was excavated from a depth of 1.5 m in developed karst areas and transported to the laboratory. The particle size distribution was determined using a screening method, and the soil was characterized in terms of its liquid and plastic limits, compaction, and chemical composition. The soil sampling and treatment processes are illustrated in Fig. 1, and the particle size distribution is provided in Table 1. Just 0.39% of the soil passed through the 0.075 mm sieve, and the proportion of particles with sizes of 2–5 mm (i.e. gravel) exceeded 50%. The non-uniformity coefficient exceeded 5, and the curvature coefficient ranged from 1 to 3. Thus, the collected soil was identified as a well-graded fine breccia soil with a particle composition of silty clay. The soil's bulk density (1.69 g/cm^3) was measured by drying and weighing, with a specific gravity and porosity of 2.52 and 32%, respectively. After drying, crushing, and passing the soil through a 0.5 mm sieve, the fine-grained components were determined using a combined liquid–plastic limit tester, with the plastic and liquid limits being 15.1% and 29.3%, respectively.

We prepared five soil samples with moisture contents of ±2% and ±4%, taking the measured plastic limit of the soil as the median. Compaction tests were performed on these samples to construct a compaction curve (Fig. 2). The optimal moisture content and maximum dry density of the 1.5-m-layer soil were determined to be 15.6% and 1.85 g/cm^3, respectively. The

Fig. 1 Soil collection and basic property analysis

chemical composition was determined using the X-ray fluorescence spectroscopy (Fig. 3).

Table 1 Soil particle size distribution (percentage of particles smaller than a certain size)

Particle size (mm)	Content (%)
10	99.78
5	73.90
2	30.98
1	15.79
0.5	7.60
0.25	3.84
0.1	0.82
0.075	0.39

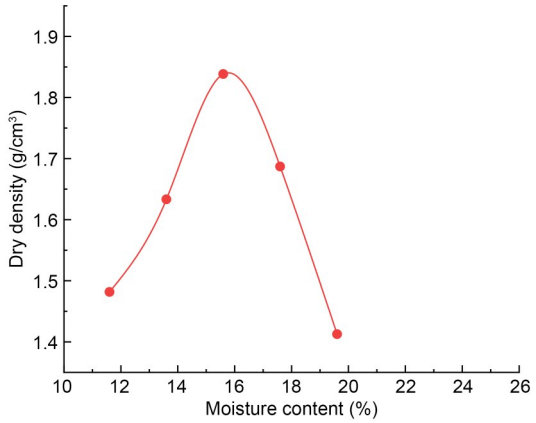

Fig. 2 Compaction curve of the soil

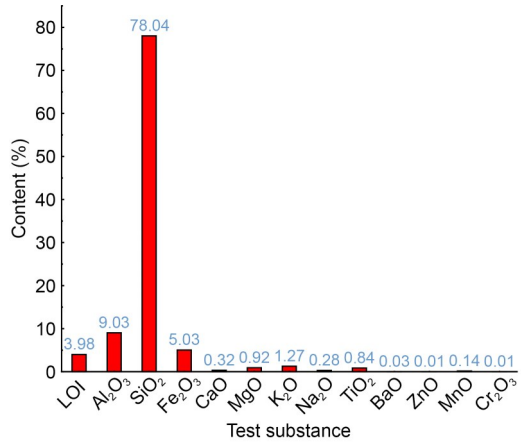

Fig. 3 Main chemical components of the soil (LOI: loss on ignition)

2.2 Test methods

Dry–wet cycles have a long-term impact on the internal structure and mechanical properties of soil. Two basic variables, the confining pressure and the number of dry–wet cycles, as well as two selective variables, the initial moisture content and compaction degree, were used to conduct undrained and unconsolidated triaxial shear tests (UU). A single-variable parallel comparison test was employed using on-site and railway subgrade engineering characteristics. Representative samples were selected for microstructural analysis with SEM imaging. Confining pressures of 150, 250, and 350 kPa were applied, considering the typical stress state of the railway subgrade and the range of commonly used confining pressures. Prior research suggests that the internal structure and deformation characteristics of soil reach a stable state after approximately five dry–wet cycles (Liu, 2015). Tests were therefore conducted after zero, two, four, and six dry–wet cycles. Moisture content measurement aimed to determine the optimal moisture content within 2% (±2%). The degree of compaction was based on the standard requirement that the degree of compaction of railway subgrade fill in China should be at least 90%. Considering the requirements for increased compaction in heavy-duty areas, compaction degrees of 93%, 95%, and 97% were selected. The experimental design is illustrated in Fig. 4.

Triaxial testing was performed using an automated apparatus (TSZ-1). The soil was crushed, dried, and passed through a 0.5 mm sieve. Water was added according to the initial moisture content requirements, and the samples were cured for 24 h. In accordance with the test specifications, each soil sample was placed and compacted in a cylindrical mold, producing a test specimen with dimensions of Φ39.1 mm×80.0 mm.

For the dry–wet cycles, the soil sample was placed in a three-petal mold saturator, placed in a vacuum, saturated in a saturation pot, and left to stand for 24 h to ensure sufficient saturation. The saturated sample was then held at room temperature (approximately 25 °C) for 24 h for natural air drying. The sample was placed in a closed box at night to simulate the higher evaporation rate during daytime. The sample was taken out of the box in the morning and air-dried at room temperature to complete one dry–wet cycle. The above process was repeated for the desired number of cycles. The sample preparation and testing procedures are illustrated in Fig. 5.

For SEM analysis, each sample was broken apart and transferred to a small cube with a side length of 5 mm. The cubic test block was placed into an aluminum

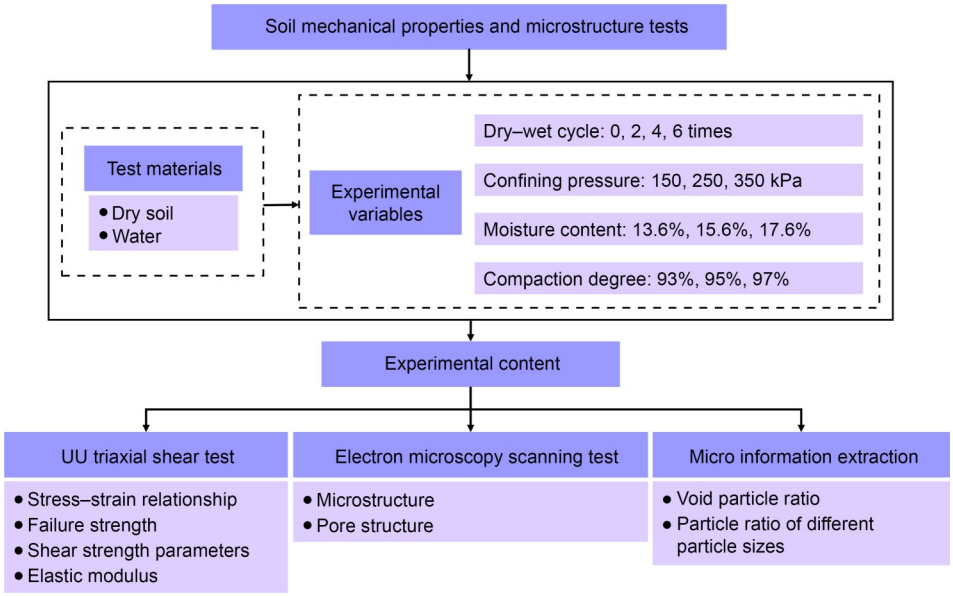

Fig. 4 Experimental procedure

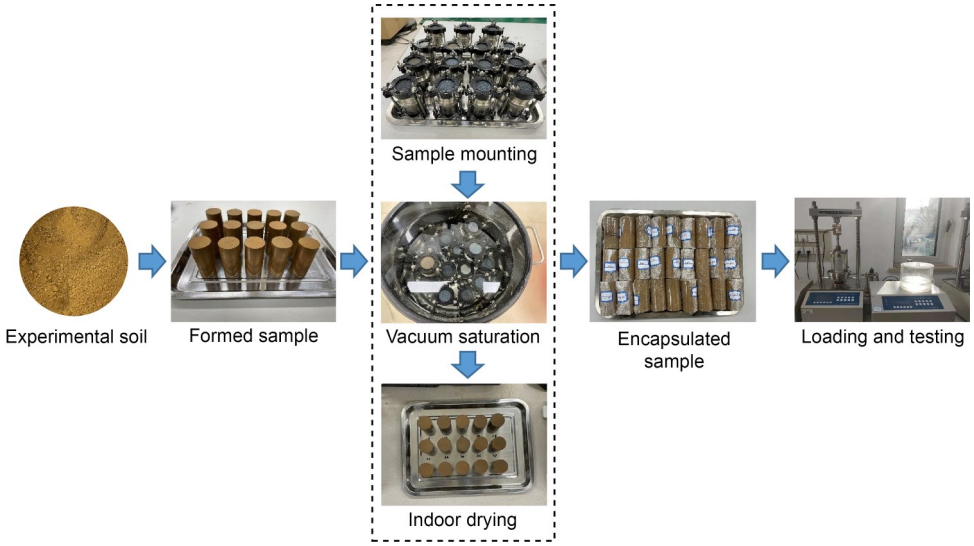

Fig. 5 Sample formation for triaxial shear tests after dry–wet cycles

box and oven-dried for 48 h to ensure the complete evaporation of moisture from the pore space. The sample surface was blow-dried and vacuum-sprayed with gold, and then imaged using an E5200 SEM. The Image Pro Plus 6.0 (IPP.V6) was used to adjust the color rendering of the target object based on imaging results. Color separation selection tools were used to select the target object, and data collectors and measurement tools were used to extract quantitative information for the selected area. The experimental and data extraction processes are illustrated in Fig. 6.

3 Results and discussion

3.1 Effects of dry–wet cycles on soil mechanical properties

3.1.1 Stress–strain relationship

Fig. 7 shows the deviatoric stress–strain curves obtained for different samples. For a constant compaction degree (Figs. 7a–7c) or initial moisture content (Figs. 7f–7h), the soil samples exhibited stress hardening, with the peak stress increasing with increasing

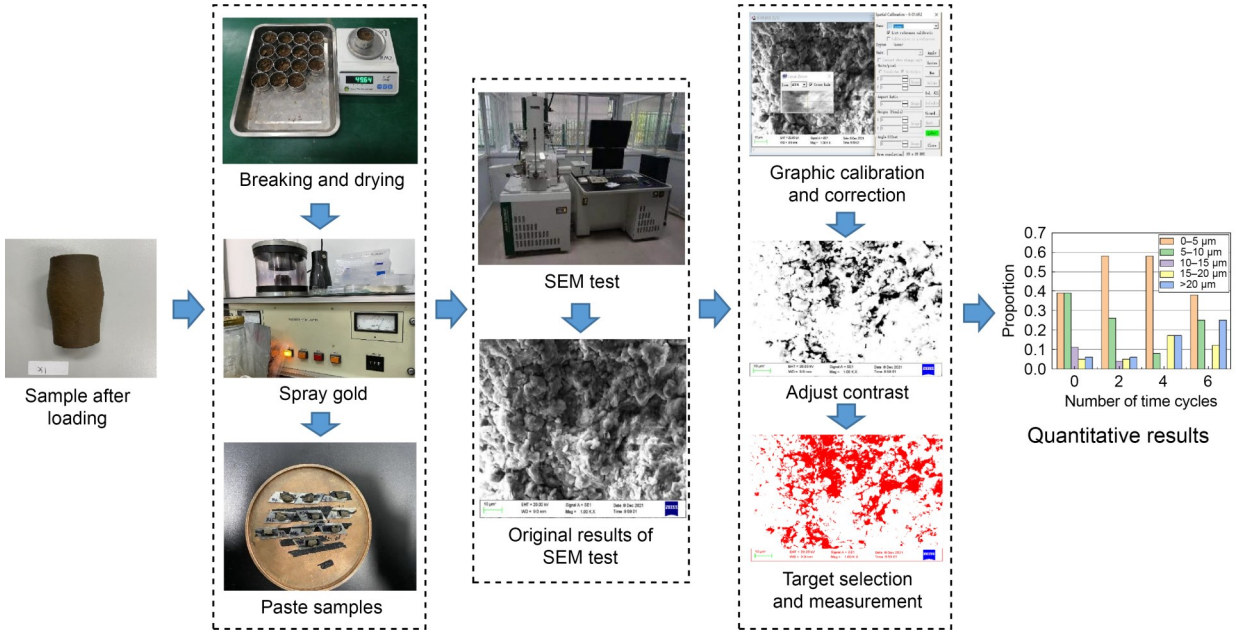

Fig. 6 Illustration of the SEM work and related data extraction procedures

confining pressure. For example, at confining pressures of 150, 250, and 350 kPa, the samples with an initial moisture content of 15.6% (Figs. 7f–7h) and zero dry–wet cycle exhibited peak stresses of 433.90, 544.04 (+25%), and 798.15 (+47%) kPa, respectively. At a constant confining pressure (Figs. 7b, 7d, and 7e) or compaction degree (Figs. 7a–7c), the peak stress generally decreased as the number of dry–wet cycles increased.

At a constant confining pressure of 250 kPa (Figs. 7b, 7d, and 7e), the peak stress typically increased with increasing compaction degree. For example, after two dry–wet cycles, the peak stresses of the samples with compaction degrees of 93%, 95%, and 97% were 439.9, 580.8, and 753.1 kPa, respectively. At 97% compaction (Fig. 7e), samples with different numbers of dry–wet cycles exhibited similar trends, and the curves became more similar. In other words, increasing the compaction degree reduced the detrimental impact of dry–wet cycles on soil performance.

At a given compaction degree, the peak stress decreased as the initial moisture content increased (Figs. 7g, 7i, and 7j). For example, at zero dry–wet cycle and confining pressure of 250 kPa, the peak stresses were 769.80, 544.04 (−29%), and 326.32 (−40%) kPa for initial moisture contents of 13.6%, 15.6%, and 17.6%, respectively. In addition, the spacing between the curves of samples with initial moisture content of 13.6% after different numbers of dry–wet cycles was smaller than that of samples with initial moisture content of 15.6% or 17.6%; this suggests that the sample with a slightly lower initial moisture content than the optimal value was more resistant to cycling-induced degradation under the same conditions.

3.1.2 Failure strength

The failure strength of engineering soil that exhibits stress hardening is typically considered to be equal to the deviatoric stress at a strain of 15%. As shown in Fig. 8a, at 15.6% initial moisture, the failure strength increased with increasing compaction degree, although the difference between the 95% and 97% samples was generally smaller than that between the 93% and 95% samples. At a constant confining pressure, the failure strength increased with the increasing compaction degree (Fig. 8a) and decreased with the increasing number of dry–wet cycles (Fig. 8b). The decrease with the number of dry–wet cycles was relatively small at 97% compaction degree compared to that at 93% or 95% compaction degree, which indicates that a higher compaction degree provides better resistance to dry–wet cycle-induced degradation.

Figs. 8c and 8d show that increasing the initial moisture content gradually decreased the failure strength at a constant compaction degree. Within six dry–wet cycles, the failure strength decreased and the decline stabilized for medium and low confining pressures, but

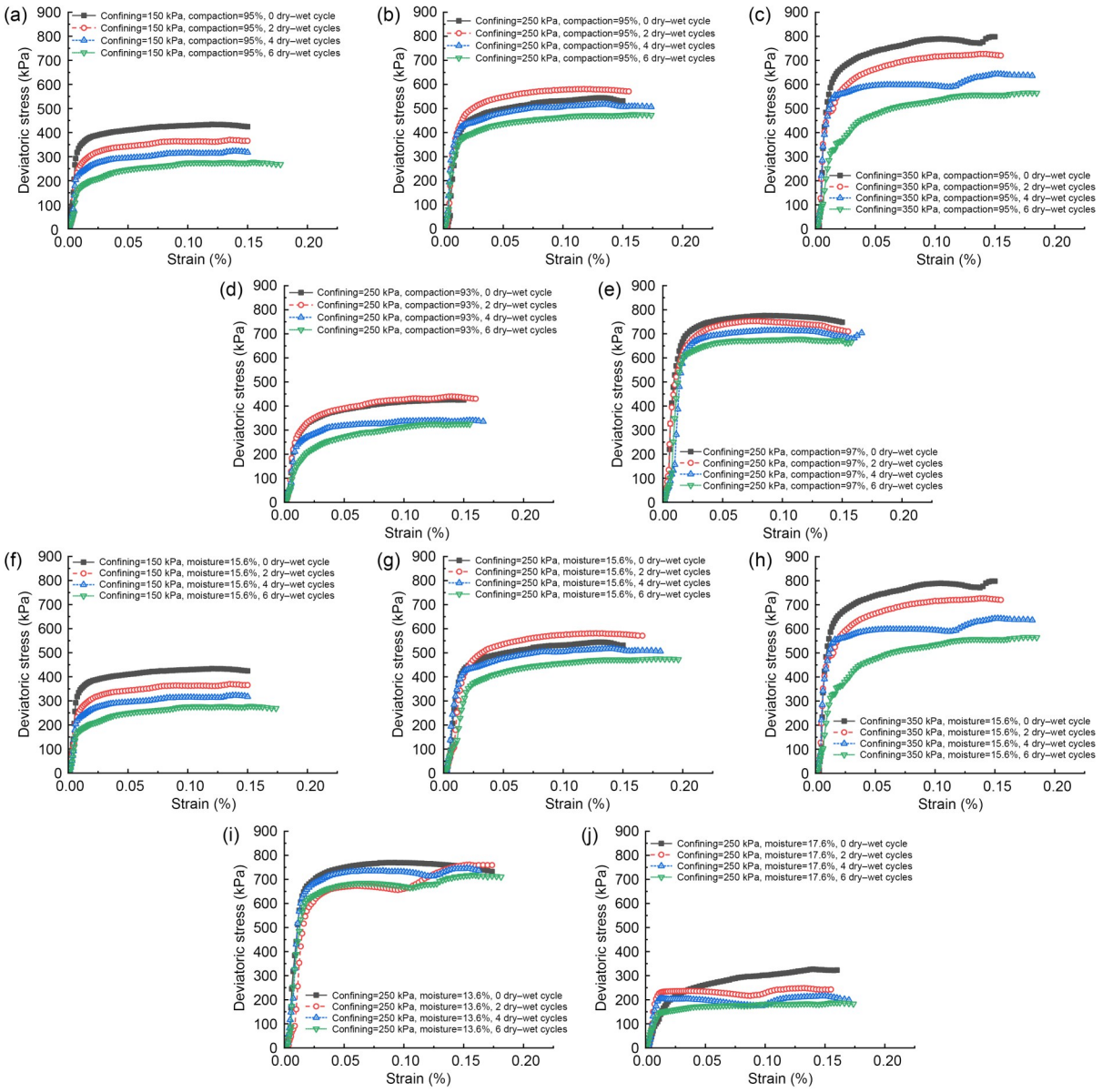

Fig. 7 Stress–strain curves during triaxial shear testing of different samples with different parameters: (a–c) confining pressures of 150 (a), 250 (b), and 350 (c) kPa at a constant compaction degree (95%); (d, e) compaction degrees of 93% (d) and 97% (e) at a constant confining pressure (250 kPa); (f–h) confining pressures of 150 (f), 250 (g), and 350 (h) kPa at a constant initial moisture content (15.6%); (i, j) initial moisture contents of 13.6% (i) and 17.6% (j) at a constant confining pressure (250 kPa). Each plot shows curves for samples after zero, two, four, and six dry–wet cycles

the decline continued to increase for a high confining pressure. The failure strength at different initial moisture contents decreased and finally stabilized with the increasing number of dry–wet cycles. Samples with initial moisture contents of 13.6%, 15.6%, and 17.6% and dry–wet cycle counts of zero (six) had failure strengths of 769.80 (718.65), 544.03 (475.48), and 326.32 (187.88) kPa, respectively. Thus, after six dry–wet cycles, the failure strength decreased by 6.6%, 12.6%, and 42.4%, respectively; that is, the magnitude of the decrease became larger with increasing moisture content.

3.1.3 Shear strength parameters

The main indicators of soil shear strength, which are the cohesion (C) and internal friction angle (φ), were determined by analyzing the triaxial test data with Mohr's circle method. Fig. 9 shows that the cohesion

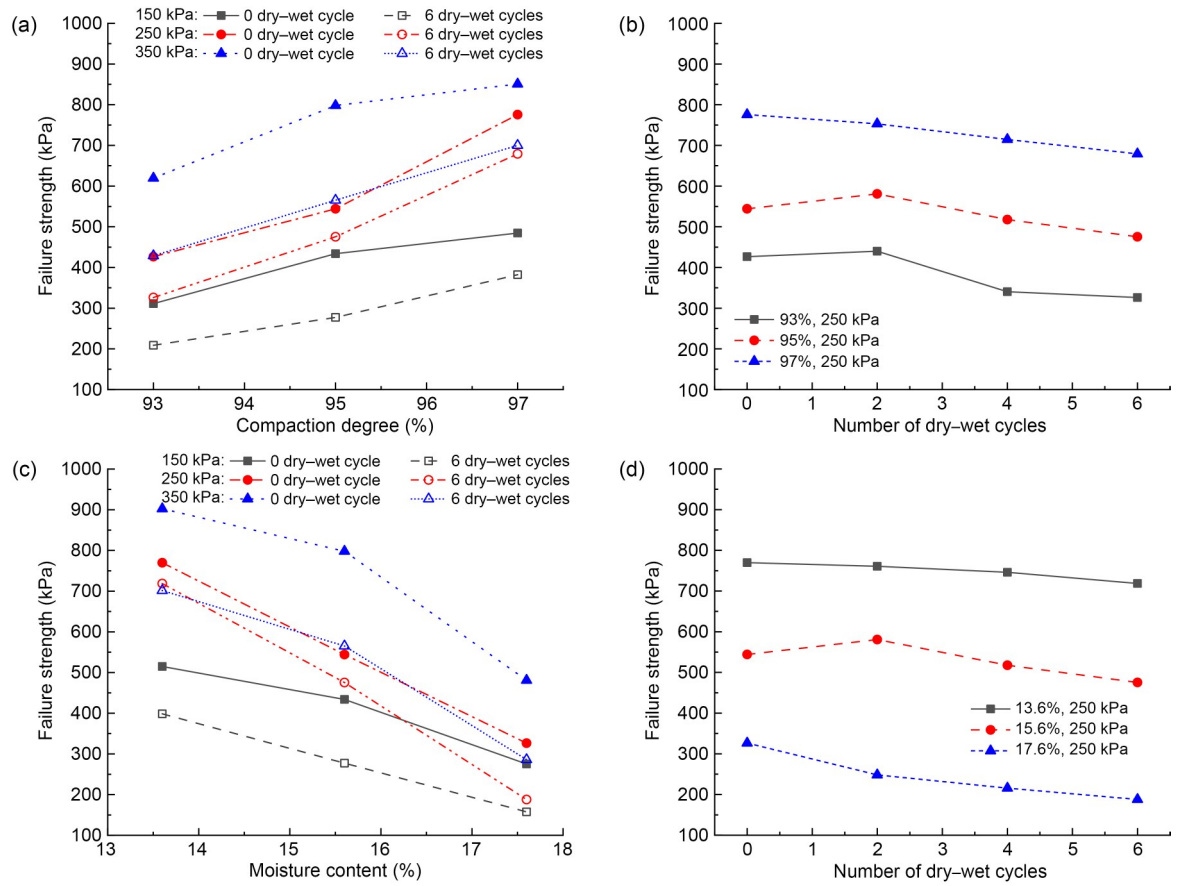

Fig. 8 Failure strength curves from triaxial testing of different soil samples: (a) effects of compaction degree and confining pressure; (b) effects of compaction degree and number of dry–wet cycles; (c) effects of initial moisture content and confining pressure; (d) effects of initial moisture content and number of dry–wet cycles

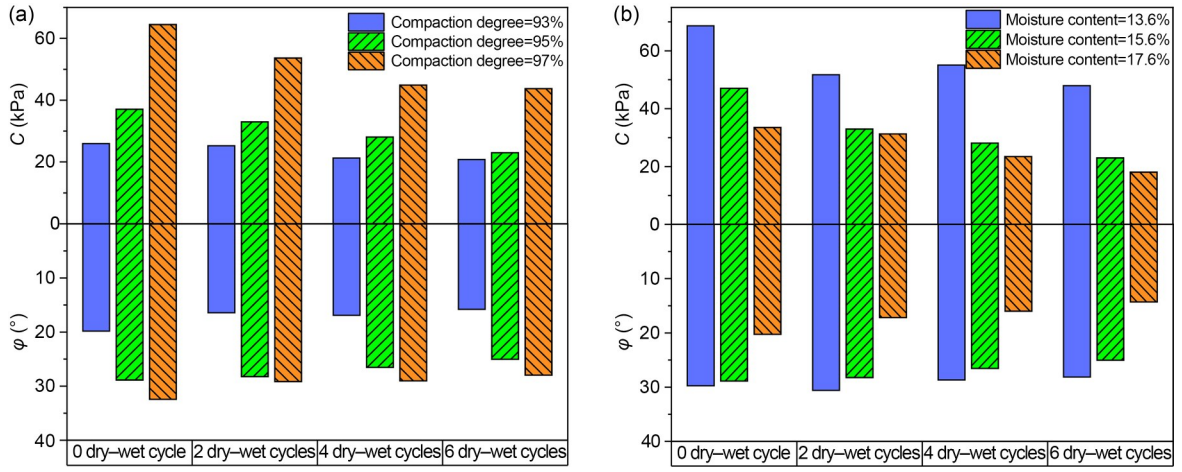

Fig. 9 Effects of (a) compaction degree and number of dry–wet cycles and (b) moisture content and number of dry–wet cycles on shear strength

and internal friction angle decreased with the increasing number of dry–wet cycles, and stabilized at different compaction degrees and initial moisture contents. The overall decrease in φ was negatively correlated with the compaction degree. The φ values of samples compacted at low pressures initially increased but decreased over the long term, possibly because water drove the movement of internal soil particles during

dry–wet cycles. The connections between particles shifted from relatively-ordered to disordered, and then rearranged along the water transport channels. This caused a slight increase in φ followed by a decrease over time. For example, at 93% compaction degree, after decreased by 17.1%, the φ value increased by 2.9% after four dry–wet cycles, and then decreased by 6.5% after six dry–wet cycles. This trend was less likely to occur at a high compaction degree.

Fig. 9b shows how, at an unideal initial moisture content, the cohesion occasionally increased with the number of dry–wet cycles but overall showed a decreasing trend. When the initial moisture content was close to or greater than the optimal value, the cohesion decreased with increasing dry–wet cycles. This may be due to how the soil evolves toward the liquid-limit state at moisture contents greater than the optimal value, and the fact that dry–wet cycle increases the pore space occupied by free water, thus reducing the cohesion. At different moisture contents, the overall φ value of the soil decreased. At a constant number of dry–wet cycles, φ decreased steadily with increasing moisture content.

3.1.4 Elastic modulus

The elastic modulus can be determined either by fitting the tangent modulus to the elastic straight-line segment of the deviatoric stress–strain curve, or by extracting the ratio of deviatoric stress to the strain increment at 1.5% strain. In this study, we used the latter method. Figs. 10a and 10b show that, for a constant confining pressure and initial moisture content, the elastic modulus increased with increasing compaction degree. The increase of the elastic modulus between 95% and 97% compaction degrees was generally greater than that between 93% and 95% compaction degrees. Moreover, the elastic modulus decreased slightly as the number of dry–wet cycles increased.

Figs. 10c and 10d show that, for a constant compaction degree and confining pressure, the elastic modulus decreased as the initial moisture content increased. The

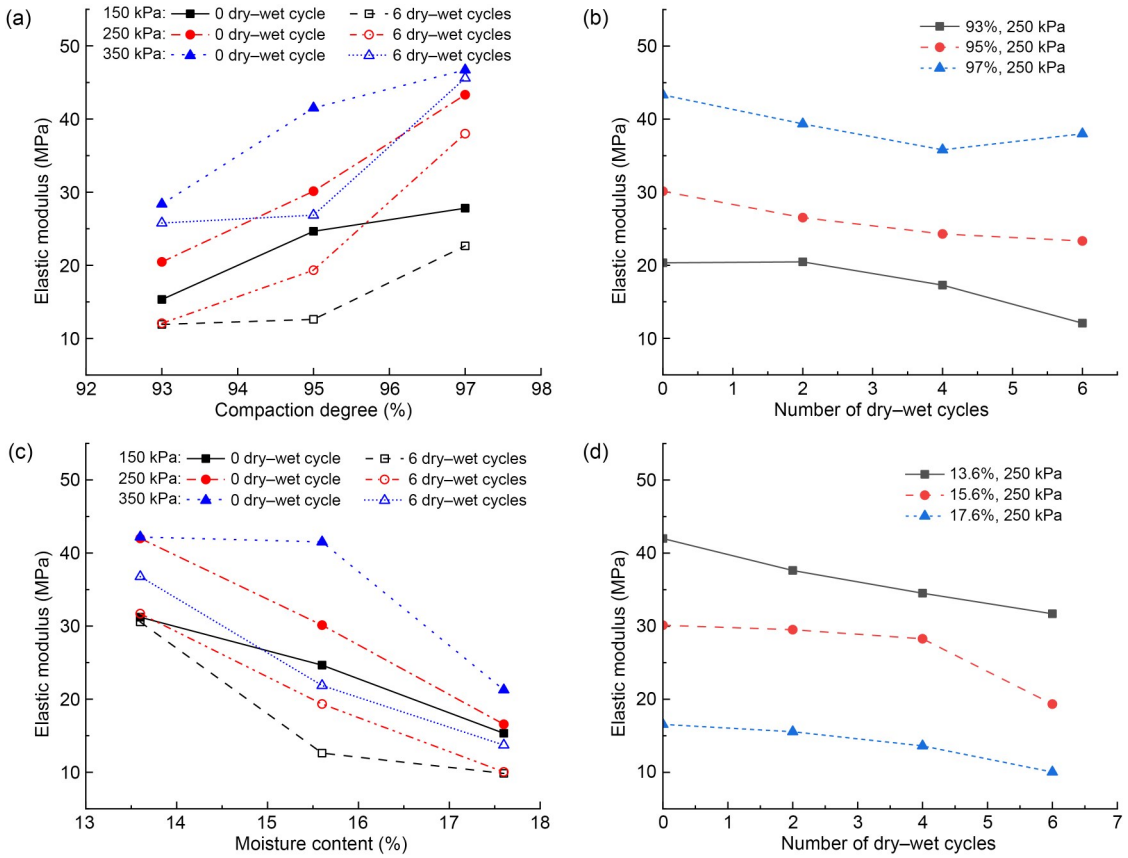

Fig. 10 Effects of (a) compaction degree and confining pressure, (b) compaction degree and number of dry–wet cycles, (c) initial moisture content and confining pressure, and (d) initial moisture content and number of dry–wet cycles on elastic modulus

reduced proportion of the elastic modulus between 13.6% and 17.6% moisture contents at 350 kPa confining pressure was lower than those under other conditions. This might be because the magnitude of the decrease in elastic modulus caused by a slight increase in moisture content is reduced with increasing confining pressure. At 150 kPa confining pressure and zero dry–wet cycle, the elastic moduli at initial moisture contents of 13.6%, 15.6%, and 17.6% were 31.21, 24.65 (−21%), and 15.33 (−38%) MPa, respectively. At 150 kPa confining pressure, six dry–wet cycles, and initial moisture contents of 13.6%, 15.6%, and 17.6%, the elastic moduli were 30.57, 12.61, and 9.84 MPa, respectively. Compared to those observed at the same moisture content and zero dry–wet cycle, these values were 2.06%, 48.84%, and 35.83% lower, respectively.

3.2 Effects of number of dry–wet cycles on soil microstructure

Fig. 11 shows variable-magnification SEM images of the soil samples. Figs. 11a–11d demonstrate that, after zero to two dry–wet cycles at a constant initial moisture content and compaction degree, many fine particles have adhered to the sample surface in large-particle-size clusters or are embedded in the pores. With the increasing number of dry–wet cycles, the number of fine particles decreased, while the pores and voids became larger and deeper, exposing the rounded boundaries of the larger particles. Figs. 11e–11g suggest that, at a constant compaction degree and zero dry–wet cycle, the sample with 13.6% initial moisture content had more plate-like and coarse angular particles than the higher-moisture content samples. The boundary angles were clear and uneven, and cracks with larger angles were observed between the particles. This could be the reason for the larger φ values. As the initial moisture content was increased further, the angular boundaries of the coarse particles softened, and some boundaries changed from an angular to a honeycomb shape, with smaller and more rounded cracks and pores, resulting in a more uniform shape.

Figs. 11h–11j show that, for a constant initial moisture content and zero dry–wet cycle, the pores

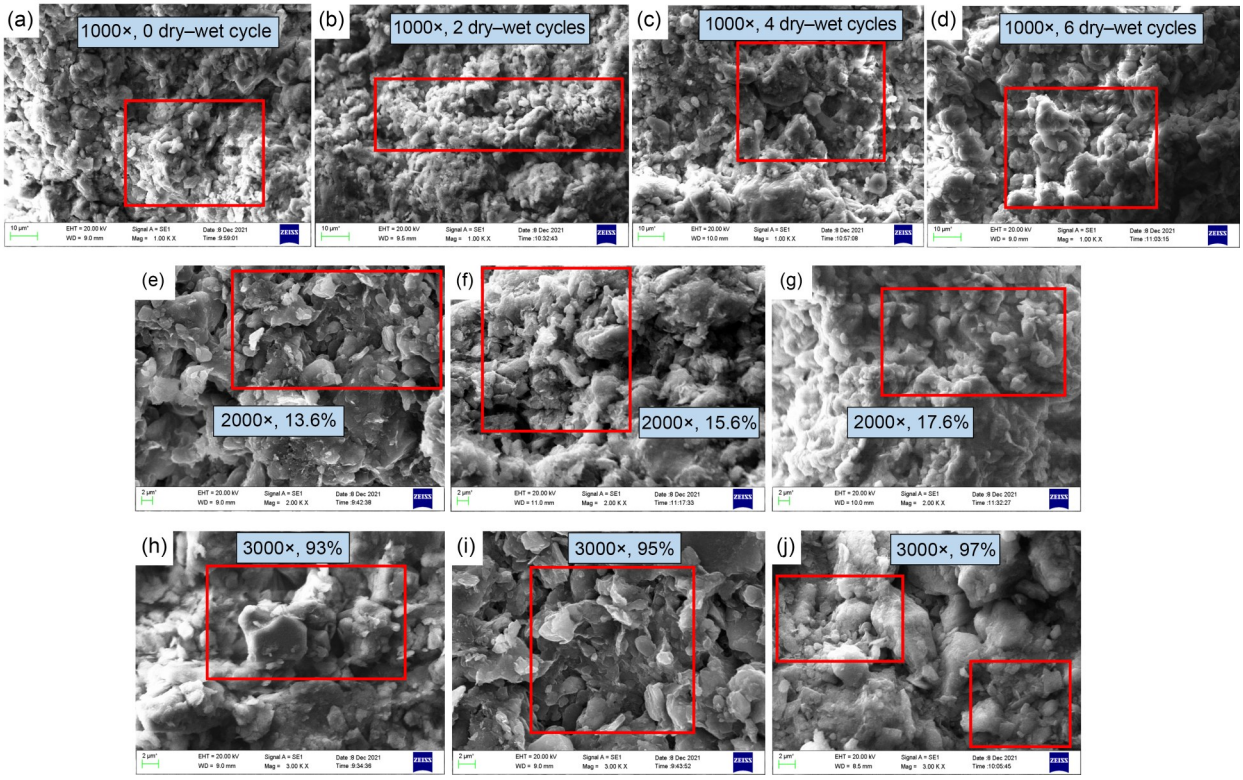

Fig. 11 SEM images of different soil samples: (a–d) effects of number of dry–wet cycles (zero, two, four, and six, respectively; 1000× magnification); (e–f) effects of initial moisture content (13.6%, 15.6%, and 17.6%, respectively; 2000× magnification); (h–j) effects of compaction degree (93%, 95%, and 97%, respectively; 3000× magnification)

and cracks observed in the samples with smaller compaction degrees were deeper; moreover, larger particle size clusters and stepped skeleton connection structures were observed. As the compaction degree increased, the particle morphology changed from smooth to flat, with more plate- and sheet-like particles, and fewer (but clearer) cracks. When the compaction degree increased to 97%, the number of small particles attached to soil aggregates decreased, and these particles became more embedded in the cracks; that is, the number of pores and holes decreased. The undulation between the large skeleton particles was gentle, with no stepped structure observed.

Figs. 12 and 13 show the results of SEM image processing using the IPP.V6. The proportion of internal pores increased substantially after the first two cycles and then stabilized. At zero dry–wet cycle, the proportion of particles within each particle size range was relatively balanced, with finer particles (and fewer coarse particles) being observed. With an increasing number of dry–wet cycles, the proportion of fine particles decreased, and the proportion of coarse particles increased. The pore–particle ratio diagrams of samples with different initial moisture contents indicate that the lowest porosity and highest density were obtained at 15.6% initial moisture content; this is due to the proximity of this initial moisture content to the optimal value. However, samples with 13.6% and 17.6% initial moisture contents had higher pore ratios. At a low initial moisture content, the particle sizes were concentrated at 5–10 μm, while the proportion of other sizes was much lower, with the size distribution being relatively uneven. At medium and high initial moisture contents, fine particles dominated, with larger particles being less abundant than at a low initial moisture content. This may be related to the increased free water content inside large particles at high initial moisture contents, which promotes disintegration into smaller particles.

The pore–particle ratio decreased with increasing compaction degree, which improved the overall stress experienced by the samples with high compaction degrees. At low compaction degrees, the overall content of large particles was relatively high, and the skeleton was relatively loose. At 95% compaction degree, the content of large particles decreased, the content of medium (10–15 μm) particles decreased to zero, and the content of small (5–10 μm) particles increased substantially. This may be due to the fragmentation of the loose large particles during compaction, which would increase the content of small particles. With a further

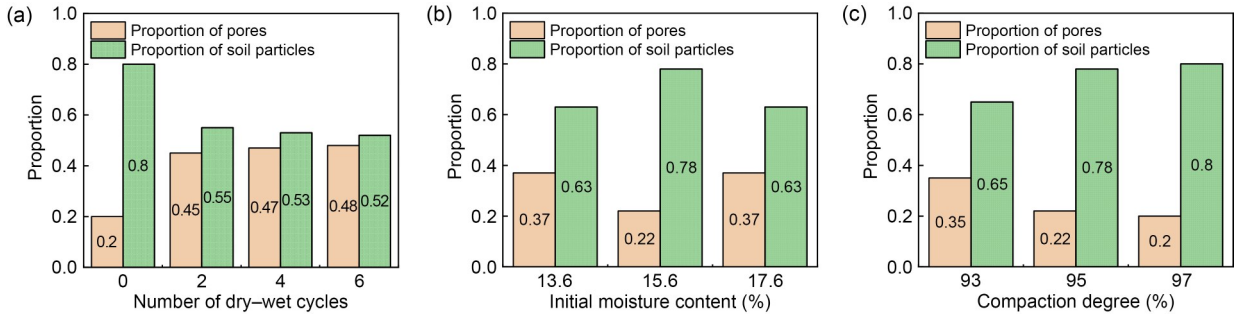

Fig. 12 Effects of (a) number of dry–wet cycles, (b) initial moisture content, and (c) compaction degree on the pore–particle ratio

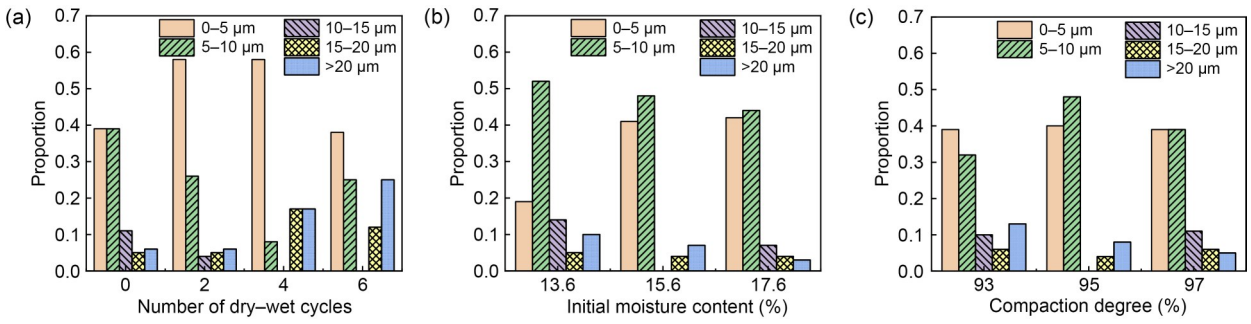

Fig. 13 Effects of (a) number of dry–wet cycles, (b) initial moisture content, and (c) compaction degree on the proportion of particles in different size ranges

increase in compaction degree, the content of small particles decreased; furthermore, medium particles reappeared, which resulted in a more uniform distribution of particle size.

3.3 Correlation between macroscopic and microscopic properties of soil, and normalized expression of stress characteristics under dry–wet cycles

3.3.1 Correlation between macroscopic and microscopic properties of soil

Table 2 summarizes the results of the triaxial shear tests and SEM imaging for different sample classes. When the initial moisture content and the number of dry–wet cycles remained unchanged, increasing the compaction degree increased the peak value of the stress–strain curve; that is, the mechanical performance was enhanced. With increasing compaction degree, the degree of embedding, particle size distribution balance, and large particle skeleton density improved to varying degrees. Therefore, the stress performance and index parameters became more conducive to subgrade stability, and more resistant to dry–wet cycle-induced degradation. Thus, given an appropriate compaction degree, we can expect an improvement in railway subgrade performance despite frequent rainfall conditions. With increasing moisture content, the angular boundaries of the soil particles gradually blurred and became more ellipsoidal/spherical. Moreover, the angle between the particles was negatively correlated with the skeleton

Table 2 Summary of soil properties and structural characteristics under different working conditions

Variable	Value	Microscopic feature	Stress peak	Failure strength	Cohesion	φ	Elastic modulus
Compaction degree	93%	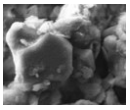	Small	Small	Small	Small	Small
	95%	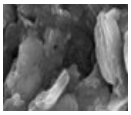	Medium	Medium	Medium	Medium	Medium
	97%		Large	Large	Large	Large	Large
Initial moisture content	13.6%	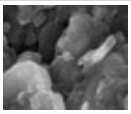	Large	Large	Large	Large	Large
	15.6%		Medium	Medium	Medium	Medium	Medium
	17.6%		Small	Small	Small	Small	Small
Number of dry–wet cycles	0		Large	Large	Large	Large	Large
	2		Medium	Medium	Medium	Medium	Medium
	4	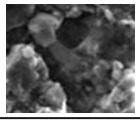	Small	Small	Small	Small	Small

embedding degree, and positively correlated with the stacking degree of the contact skeleton. The proportion of small and medium particles also increased, with some large skeleton particles disintegrating into smaller particles, thereby causing mechanical property deterioration.

In summary, when selecting fine breccia soil for foundation treatment, soil with a higher compaction degree and slightly lower initial moisture content should be selected for use as fill. Frequent rainfall in the area is more conducive to durability and stability, and greater cohesion and φ enable resistance to the loss of soil particles to hidden caves and karst channels under the action of seepage.

3.3.2 Normalization characteristics of soil under dry–wet cycles

Different methods have been proposed for normalizing the mechanical properties of soil. Among them, Konder's normalization method (Duncan and Chang, 1970), which is based on hyperbolic equations and normalization factors, fits the results of static triaxial tests and yields reasonable normalization conditions. The related expressions are as follows:

$$\sigma_1-\sigma_3=\varepsilon_1/\sigma_3, \tag{1}$$

$$\varepsilon_1/(\sigma_1-\sigma_3)=a\varepsilon_1+b, \tag{2}$$

where a is the reciprocal of the ultimate deviator stress $(\sigma_1-\sigma_3)_u$ for a given confining pressure, ε_1 is the axial strain, and b is the reciprocal of the initial tangent modulus E_i. Eq. (2) shows that the linear relationship between the ratio of axial strain to the deviator stress and the axial strain has a slope of a and a longitudinal intercept of b. At different confining pressures (σ_3), the a and b normalization results for the same soil sample differ. To obtain the stress–strain normalization relationship at different confining pressures, one can multiply both sides of Eq. (2) by a normalization factor A:

$$A\varepsilon_1/(\sigma_1-\sigma_3)=Aa\varepsilon_1+Ab. \tag{3}$$

Further,

$$M=Aa,\ N=Ab, \tag{4}$$

where M and N are constants, indicating that the normalization condition is essentially a positive proportional relationship between the normalization factor A, ultimate deviator stress $(\sigma_1-\sigma_3)_u$, and initial tangent modulus E_i. The commonly-used normalization factors and their conditions are listed in Table 3.

Table 3 Statistical analysis parameters of the fitting results

Normalization factor	Normalization condition
σ_3	$(\sigma_1-\sigma_3)_u$, $E_i \propto \sigma_3$
σ_m	$(\sigma_1-\sigma_3)_u$, $E_i \propto \sigma_m$
$(\sigma_1-\sigma_3)_u$	$(\sigma_1-\sigma_3)_u \propto E_i$
$(\sigma_3)^n$	$(\sigma_1-\sigma_3)_u$, $E_i \propto (\sigma_3)^n$

σ_m is the average principal stress

Table 3 suggests that few limiting conditions exist when the ultimate deviator stress is used as a normalization factor. Therefore, we decided to use the ultimate deviator stress as a normalization factor; accordingly, we fit the stress–strain curves of a 1.5-m-buried soil sample with a compaction degree of 95% and initial moisture content of 15.6%, at confining pressures of 150, 250, and 350 kPa. Eq. (2) was applied to fit the stress–strain curves in Figs. 7a–7c. Data points near the starting point of the curve were removed during the loading process. The results are shown in Fig. 14, and the fitting parameters are summarized in Table 4.

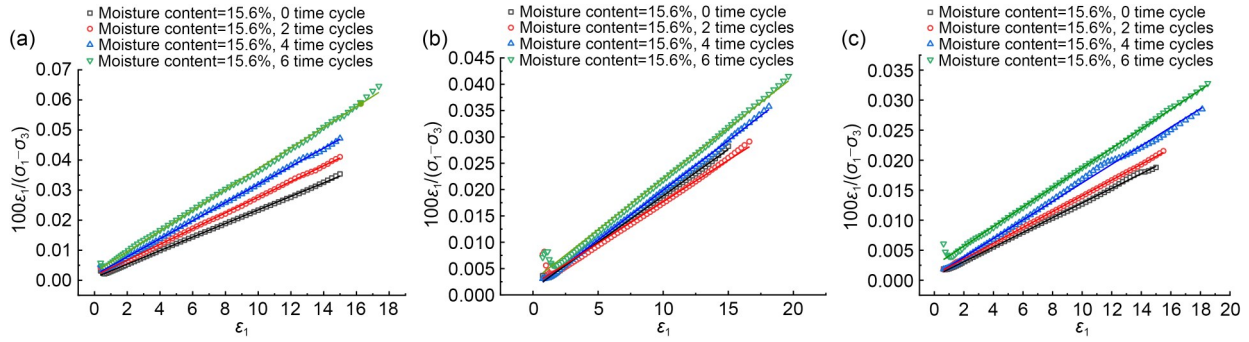

Fig. 14 Relationship between $\varepsilon_1/(\sigma_1-\sigma_3)$ and ε_1 with different numbers of dry–wet cycles at confining pressures of 150 kPa (a), 250 kPa (b), and 350 kPa (c)

Table 4 Relationship-fitting parameters of $\varepsilon_1/(\sigma_1-\sigma_3)$ and ε_1

σ_3 (kPa)	Cycle No.	a ($\times10^3$)	b ($\times10^5$)	$(\sigma_1-\sigma_3)_u$ (kPa)	E_i (MPa)	R^2
150	0	2.25	0.88	444.44	113.97	0.9998
150	2	2.62	1.49	381.68	67.33	0.9998
150	4	3.01	1.77	332.23	56.56	0.9996
150	6	3.44	2.67	290.70	37.46	0.9991
250	0	1.76	0.72	568.18	139.20	0.9991
250	2	1.58	1.89	632.91	52.85	0.9849
250	4	1.89	0.99	529.10	100.56	0.9995
250	6	1.93	2.72	518.13	36.70	0.9934
350	0	1.22	0.64	819.67	155.46	0.9993
350	2	1.31	0.91	763.36	109.33	0.9999
350	4	1.55	0.76	645.16	131.71	0.9975

When $(\sigma_1-\sigma_3)_u$ is zero, E_i is also zero. Linear fitting was performed on the data of $(\sigma_1-\sigma_3)_u$ and E_i at different confining pressures and dry–wet cycle numbers, with the initial value of the fitting curve being (0, 0). The obtained fit is shown in Fig. 15, and the fitting expression is given in Eq. (5). The coefficient of determination (R^2) for this curve is 0.88. Linear fitting was performed for the relationship between the ultimate deviator stress and the confining pressure at zero dry–wet cycle. The results are shown in Fig. 16 and Eq. (6) (R^2=0.97).

$$(\sigma_1-\sigma_3)_u=0.00552E_i, \tag{5}$$

$$(\sigma_1-\sigma_3)_{u0}=1.88\sigma_3+141.73, \tag{6}$$

where $(\sigma_1-\sigma_3)_{ui}$ represents the ultimate deviator stress after the ith dry–wet cycle. The residual strength ratio after the ith dry–wet cycle is defined as $Q_i=(\sigma_1-\sigma_3)_{ui}/(\sigma_1-\sigma_3)_{u0}$ and reflects the ability of the soil to resist degradation by dry–wet cycles. The larger the value of Q_i, the better the soil can resist the degradation effect of dry–wet cycles and the better suited it is to use in areas with high rainfall. When $(\sigma_1-\sigma_3)_{ui}$ is used as the fitting normalization factor, the fitting expression becomes

$$\varepsilon_1(\sigma_1-\sigma_3)_{ui}/(\sigma_1-\sigma_3)=(\sigma_1-\sigma_3)_{ui}a\varepsilon_1+(\sigma_1-\sigma_3)_{ui}b. \tag{7}$$

Based on the residual strength ratio and Eqs. (5) and (6), the relationship between the stress characteristics of fine breccia soil in karst areas under dry–wet cycles can be expressed as follows:

$$\sigma_1-\sigma_3=Q_i\varepsilon_1(1.88\sigma_3+141.73)/(0.00552+\varepsilon_1). \tag{8}$$

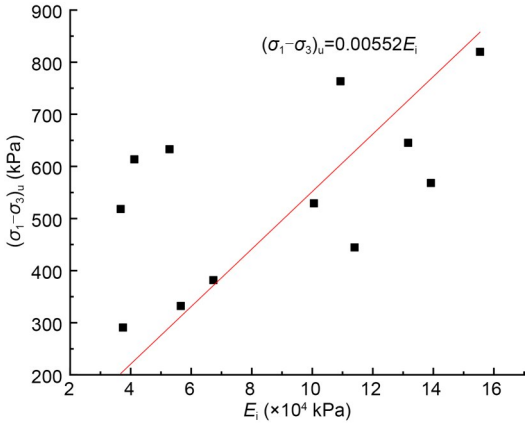

Fig. 15 Relationship between $(\sigma_1-\sigma_3)_u$ and E_i

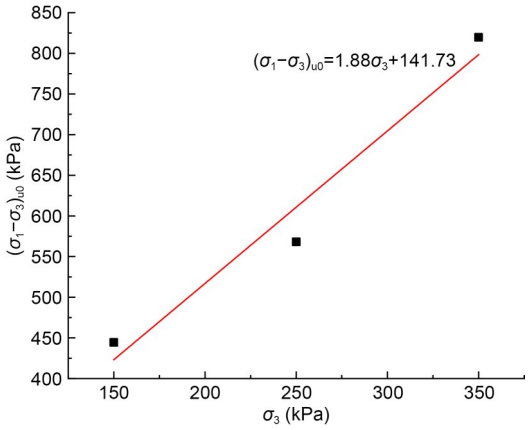

Fig. 16 Relationship between $(\sigma_1-\sigma_3)_{u0}$ and σ_3

4 Conclusions

Triaxial shear tests and SEM were used to study the mechanical properties and microscopic characteristics of fine breccia soil from karst areas. These tests facilitated analysis of the mechanical properties, microstructures, micro-to-macro correlations, and damage models of in situ railway subgrade fill experiencing prolonged dry–wet cycles in karst areas.

The deformation behavior of the fine breccia soil in karst terrains exhibited a stress-hardening trend. The peak stress in the soil was directly correlated to the degree of compaction and confining pressure, and inversely correlated to the moisture content and number of dry–wet cycles. Soil that underwent high-pressure compaction and maintained a slightly lower initial moisture content

than the optimal value showed greater resistance to degradation from dry–wet cycles.

For soil samples that underwent high-pressure compaction, the failure strength, shear strength, and elastic modulus remained relatively unaffected by the dry–wet cycles. However, the values of these properties decreased when the water content was high, and even more so when confining pressures were high.

An increased degree of compaction improved the particle size distribution and skeleton density of the soil, enhancing the mechanical properties and performance indicators. Thus, greater soil compaction should make the railway subgrade more resistant to the erosive impact of dry–wet cycles, ensuring better stability, especially under frequent rainfall. Conversely, a rise in moisture content blurred the angular demarcations of soil particles. Increased angularity between particles led to a decline in the structural integrity of the embedded skeleton, causing larger skeletal particles to disintegrate into smaller ones, adversely impacting the soil's mechanical properties and thus railway subgrade stability.

A normalized stress–strain model was formulated from the results of the triaxial stress and SEM experiments on fine breccia soils. This model incorporates the effects of confining pressure and dry–wet cycles by integrating the residual strength ratio associated with dry–wet cycles. Overall, to mitigate the effects of dry–wet cycles and achieve higher stability when using fine breccia soil from karst areas as railway subgrade fill, we recommend techniques that yield a higher compaction degree and a moisture content close to the optimal value.

Acknowledgments

This work is supported by the National Natural Science Foundation of China (Nos. 52108377 and 51938008) and the Guangdong Basic and Applied Basic Research Foundation (No. 2023A1515010060), China.

Author contributions

Xin LI: validation; investigation; conceptualization; methodology; formal analysis; writing–original draft. Hanqing CHEN: investigation; writing–review and editing. Dong SU: funding acquisition; supervision. Xiangsheng CHEN: funding acquisition; supervision. Xiang SHEN: writing–review and editing.

Conflict of interest

The authors declare no known economic or personal competitive interests or relationships affecting the publication of this article.

Data availability

Data will be made available on request.

References

Celauro C, Corriere F, Guerrieri M, et al., 2017. Environmental analysis of different construction techniques and maintenance activities for a typical local road. *Journal of Cleaner Production*, 142:3482-3489. https://doi.org/10.1016/j.jclepro.2016.10.119

Chao ZM, Shi DD, Fowmes G, 2023. Mechanical behaviour of soil under drying–wetting cycles and vertical confining pressures. *Environmental Geotechnics*, in press. https://doi.org/10.1680/jenge.22.00048

Chen RF, Cai GJ, Dong XQ, et al., 2019. Mechanical properties and micro-mechanism of loess roadbed filling using by-product red mud as a partial alternative. *Construction and Building Materials*, 216:188-201. https://doi.org/10.1016/j.conbuildmat.2019.04.254

Deng YH, Wang SJ, Bai XY, et al., 2020. Spatiotemporal dynamics of soil moisture in the karst areas of China based on reanalysis and observations data. *Journal of Hydrology*, 585:124744. https://doi.org/10.1016/j.jhydrol.2020.124744

Drobinina E, Kovaleva T, Koriakina A, 2020. The local variation of the overlying soils geotechnical properties in the karst susceptibility assessment. *Carbonates and Evaporites*, 35(3):79. https://doi.org/10.1007/s13146-020-00615-3

Duncan JM, Chang CY, 1970. Nonlinear analysis of stress and strain in soils. *Journal of the Soil Mechanics and Foundations Division*, 96(5):1629-1653. https://doi.org/10.1061/JSFEAQ.0001458

Fang JJ, Yang XL, Feng YX, et al., 2021. True triaxial experimental study on mechanical properties of expansive soils after drying and wetting cycles. *Chinese Journal of Rock Mechanics and Engineering*, 40(5):1043-1055 (in Chinese). https://doi.org/10.13722/j.cnki.jrme.2020.0902

Feng SX, Lei HY, 2022. A settlement prediction model considering tidal loading and traffic loading of soft soil subgrade. *Computers and Geotechnics*, 144:104639. https://doi.org/10.1016/j.compgeo.2022.104639

Geng DX, Meng C, Wang J, et al., 2022. Coupling influence of rainfall infiltration and traffic load on silt roadbed. *Journal of Chongqing Jiaotong University (Natural Science)*, 41(6):98-104 (in Chinese). https://doi.org/10.3969/j.issn.1674-0696.2022.06.15

Goh SG, Rahardjo H, Leong EC, 2014. Shear strength of unsaturated soils under multiple drying-wetting cycles. *Journal of Geotechnical and Geoenvironmental Engineering*, 140(2):06013001. https://doi.org/10.1061/(ASCE)GT.1943-5606.0001032

Han J, Zhao GT, Sheng XZ, et al., 2016. Study on the subgrade deformation under high-speed train loading and water–soil interaction. *Acta Mechanica Sinica*, 32(2):233-243. https://doi.org/10.1007/s10409-015-0522-6

Hong Y, Li ZR, Tang SS, et al., 2020. Effect of average particle size on shear properties of sand and its mesomechanical

analysis. *Journal of Jilin University (Earth Science Edition)*, 50(6):1814-1822 (in Chinese). https://doi.org/10.13278/j.cnki.jjuese.20190081

Hu WL, Cheng WC, Wen SJ, et al., 2021. Effects of chemical contamination on microscale structural characteristics of intact loess and resultant macroscale mechanical properties. *Catena*, 203:105361. https://doi.org/10.1016/j.catena.2021.105361

Huang G, Zheng MX, 2021. Effect of dry-wet cycling on the residual strength characteristics of coal measure soil. *KSCE Journal of Civil Engineering*, 25(11):4184-4195. https://doi.org/10.1007/s12205-021-2147-6

Ibrahim OR, Maqbali LAA, Shaqsi MSA, 2022. Comparison between sediment material and natural subgrade material for road construction. *Key Engineering Materials*, 913: 215-226. https://doi.org/10.4028/p-yj1y51

Khalid RA, Ahmad N, Arshid MU, et al., 2022. Performance evaluation of weak subgrade soil under increased surcharge weight. *Construction and Building Materials*, 318:126131. https://doi.org/10.1016/j.conbuildmat.2021.126131

Kong XH, Wang GQ, Liang YP, et al., 2022. The engineering properties and microscopic characteristics of high-liquid-limit soil improved with lignin. *Coatings*, 12(2):268. https://doi.org/10.3390/coatings12020268

Li SY, He ZL, Zhu P, et al., 2022. Experimental study on the triaxial compression properties of coarse-grained filling soil under drying–wetting cycles. *Geofluids*, 2022(1):1452916. https://doi.org/10.1155/2022/1452916

Li W, Zeng S, Zhao J, et al., 2017. Damage characteristics of Changsha ring expressway silty clay during dry-wet cycle. *Journal of Central South University (Science and Technology)*, 48(5):1360-1366 (in Chinese). https://doi.org/10.11817/j.issn.1672-7207.2017.05.031

Li X, Bai MZ, Wei ZJ, et al., 2021. Dynamic response and stability analysis of high-speed railway subgrade in karst areas. *IEEE Access*, 9:129188-129206. https://doi.org/10.1109/ACCESS.2021.3113706

Li Y, Liu JJ, 2020. Mechanical behavior and microstructure of crude-oil-polluted structural loess in Nanjing City, China. *Journal of Porous Media*, 23(2):163-176. https://doi.org/10.1615/JPorMedia.2019027086

Li Z, Guan CH, Han M, et al., 2022. Estimation of settlement in loess-filled subgrade with consideration of lateral deformation. *Arabian Journal for Science and Engineering*, 47(4):4713-4729. https://doi.org/10.1007/s13369-021-06247-6

Lin BT, Cerato AB, 2015. Shear strength of shale weathered expansive soils along swell-shrink paths: analysis based on microscopic properties. *Environmental Earth Sciences*, 74(9):6887-6899. https://doi.org/10.1007/s12665-015-4691-1

Liu WH, 2015. Effect of Drying/Wetting on the Mechanical Behaviors of Unsaturated Soils and Study on the Constitutive Relationship of Unsaturated Soils. PhD Thesis, Dalian University of Technology, Dalian, China (in Chinese).

Lu Z, Fang R, Chen LH, et al., 2020. Long-term deformation of highway subgrade under coupling effect of traffic load and drying–wetting cycles. *International Journal of Geomechanics*, 20(2):04019168. https://doi.org/10.1061/(ASCE)GM.1943-5622.0001568

Luo YP, Meng JH, Wang DF, et al., 2022. Experimental study on mechanical properties and microstructure of metakaolin based geopolymer stabilized silty clay. *Construction and Building Materials*, 316:125662. https://doi.org/10.1016/j.conbuildmat.2021.125662

Jiang MJ, 2019. New paradigm for modern soil mechanics: geomechanics from micro to macro. *Chinese Journal of Geotechnical Engineering*, 41(2):195-254 (in Chinese). https://doi.org/10.11779/CJGE201902001

Mu K, Kong LW, Zhang XW, et al., 2016. Experimental investigation on engineering behaviors of red clay under effect of wetting-drying cycles. *Rock and Soil Mechanics*, 37(8): 2247-2253 (in Chinese). https://doi.org/10.16285/j.rsm.2016.08.016

Que Y, Zhang HY, Zhu TJ, et al., 2022. Amending foamed lightweight soil with tailings sand for embankment applications: physical properties, durability, and microstructure. *Construction and Building Materials*, 350:128912. https://doi.org/10.1016/j.conbuildmat.2022.128912

Raja K, Vishnuvardhan K, Venkatachalam S, et al., 2022. Strength and settlement of subgrade soil in southern part of Kangeyam block. *Materials Today: Proceedings*, 65:1930-1938. https://doi.org/10.1016/j.matpr.2022.05.173

Smirnova MA, Gennadiev AN, 2011. Soils of karst sinkholes in the southeast of the Belomorsk-Kuloi Plateau. *Eurasian Soil Science*, 44(2):117-125. https://doi.org/10.1134/S106422931102013X

Song BH, Han C, Chen JH, et al., 2015. Subgrade design and construction technology for saline soil area. *Applied Mechanics and Materials*, 744-746:641-646. https://doi.org/10.4028/www.scientific.net/AMM.744-746.641

Sun YQ, Meng SJ, Wang M, et al., 2021. Deterioration effect of freeze-thaw on mechanical properties of roadbed clay under unfavorable conditions. *Bulletin of Engineering Geology and the Environment*, 80(6):4773-4790. https://doi.org/10.1007/s10064-021-02203-8

Wang L, Cheng WC, Xue ZF, 2022. Investigating microscale structural characteristics and resultant macroscale mechanical properties of loess exposed to alkaline and saline environments. *Bulletin of Engineering Geology and the Environment*, 81(4):146. https://doi.org/10.1007/s10064-022-02640-z

Wang LC, 2014. Experimental study on dynamic characteristics of subgrade soil under cyclic load in karst area. *Mining and Metallurgical Engineering*, 34(3):16-18 (in Chinese). https://doi.org/10.3969/j.issn.0253-6099.2014.03.005

Wang SJ, Jiang HG, Wang ZB, et al., 2022. Evaluation of heavy roller compaction on a large-thickness layer of subgrade with full-scale field experiments. *Journal of Zhejiang University-SCIENCE A (Applied Physics & Engineering)*, 23(11):933-944. https://doi.org/10.1631/jzus.A2200201

Wen TD, Shao LT, Guo XX, 2021. Effect of hysteresis on hydraulic properties of soils under multiple drying and

wetting cycles. *European Journal of Environmental and Civil Engineering*, 25(10):1750-1762. https://doi.org/10.1080/19648189.2019.1600037

Xiao JH, Liu JK, Hou YF, et al., 2007. Experimental study on mechanical properties of rock-salt for subgrade fill material. *Journal of Engineering Geology*, 15(1):119-123. https://doi.org/10.3969/j.issn.1004-9665.2007.01.020

Xu JB, Wang YZ, Yan CG, et al., 2019. Lifecycle health monitoring and assessment system of soft soil subgrade for expressways in China. *Journal of Cleaner Production*, 235:138-145. https://doi.org/10.1016/j.jclepro.2019.06.256

Yuan KZ, Ni WK, Lü XF, et al., 2021. Permeability characteristics and structural evolution of compacted loess under different dry densities and wetting-drying cycles. *PLoS One*, 16(6):e0253508. https://doi.org/10.1371/journal.pone.0253508

Yu JJ, Chen DX, Wang H, et al., 2019. Analysis of the shear strength of granite residual soil and slope stability under wetting-drying cycles. *Journal of Xiamen University (Natural Science)*, 58(4):614-620 (in Chinese). https://doi.org/10.6043/j.issn.0438-0479.201902003

Zeng L, Yu HC, Gao QF, et al., 2022. Evolution of tensile properties of compacted red clay under wet and dry cycles. *KSCE Journal of Civil Engineering*, 26(2):606-618. https://doi.org/10.1007/s12205-021-0527-6

Zhou LJ, 2012. Subgrade stability analysis with rainfall infiltration. *Applied Mechanics and Materials*, 204-208:284-288. https://doi.org/10.4028/www.scientific.net/AMM.204-208.284